Chemical Engineering Journal 162 (2010) 151–157

Contents lists available at ScienceDirect

Chemical Engineering Journal

journal homepage: www.elsevier.com/locate/cej

Highly active CuO/OMS-2 catalysts for low-temperature CO oxidation

Xue-Song Liu[a], Zhu-Nian Jin[b], Ji-Qing Lu[a], Xiao-Xia Wang[a], Meng-Fei Luo[a,*]

[a] Key Laboratory of the Ministry of Education for Advanced Catalysis Materials, Institute of Physical Chemistry, Zhejiang Normal University, Jinhua 321004, Zhejiang, China
[b] Jinhua College of Vocation and Technology, Jinhua 321007, Zhejiang, China

ARTICLE INFO

Article history:
Received 28 January 2010
Received in revised form 9 May 2010
Accepted 11 May 2010

Keywords:
Manganese oxide octahedral molecular sieves (OMS-2)
CuO/OMS-2 catalysts
CO oxidation

ABSTRACT

Manganese oxide octahedral molecular sieves (OMS-2) were synthesized using $MnSO_4$ and $KMnO_4$ as precursors by a reflux method under acidic conditions. CuO/OMS-2 catalysts were prepared by an impregnation method and tested for CO oxidation. The synthesized OMS-2 molecular sieves were nanorods, with the cryptomelane-type structure. X-ray photoelectron spectra (XPS) and hydrogen temperature program reduction (H_2-TPR) results indicated that the OMS-2 support contained high concentration of Mn^{4+} (50%) in the OMS-2 support and an interaction between CuO and OMS-2. The CuO/OMS-2 catalysts showed higher activities for CO oxidation compared with the CuO/MnO_x catalyst. Among the CuO/OMS-2 catalysts, the highest reactivity was obtained on CuO15/OMS-2 catalyst, with a T_{90} (the lowest temperature for 90% conversion of CO) of 55 °C. The interaction between the highly dispersed CuO and OMS-2 support generates active sites for CO oxidation. CO oxidation may follow the Mars-van-Krevelen mechanism with Cu^{2+}–O^{2-}–Mn^{4+} ↔ Cu^{+}–□–Mn^{3+} + O_2 redox couple.

1. Introduction

The catalytic oxidation of CO has wide applications in indoor air cleaning, CO gas sensors, CO_2 lasers, and automotive exhaust treatment [1,2]. Precious-metal catalysts such as Au/TiO_2, Au/ZrO_2 and Pt/SnO_2 have been used for low-temperature CO oxidation [3–5]. However, due to the high cost of precious metals, more attention has been given to the use of base-metal catalysts, especially copper catalysts [6–8]. Among them, Cu–Ce–O catalysts are of special interest due to their remarkable activities that are even comparable to the noble metals [9]. Our previous work showed that Cu–Ce–O catalysts exhibited excellent activities superior to other Cu-based catalysts, due to the finely dispersed CuO species and Cu–Ce interactions [10]. Chen et al. also found that the finely dispersed CuO species were the active phase for CO oxidation [8].

Octahedral molecular sieves (OMS-2) of manganese oxides are cryptomelane-type manganese oxides, with a porous structure (0.46 nm) arising from edge sharing of 2 × 2 [MnO_6] octahedral chains to form one-dimensional tunnel structures [11,12]. Mn species in the OMS-2 material have mixed-valent Mn^{4+}, Mn^{3+}, and some Mn^{2+} sites. Divalent and trivalent transition metal ions incorporated into OMS-2 have been developed as promising catalysts for oxidation reactions [13], such as selective oxidation of benzyl alcohol, cyclohexane, as well as oxidation of methanol for fuel cell applications [14,15]. Also, Ag-OMS-2 has been reported as an active catalyst for the CO oxidation [16].

Since CuO-based catalysts show remarkable activities for CO oxidation, in the present study, CuO catalysts supported on OMS-2 (CuO/OMS-2) were prepared and tested for CO oxidation. For comparison, CuO supported on conventional MnO_x was also prepared. It was found that the CuO/OMS-2 catalysts were highly active for CO oxidation at low temperature. A possible reaction pathway for CO oxidation was also discussed.

2. Experimental

2.1. Catalyst preparation

Manganese oxide octahedral molecular sieves (OMS-2) were synthesized by a reflux method [17]. A typical synthesis was as follows: 11.33 g of $MnSO_4{\cdot}H_2O$ (0.072 mol) dissolved in 120 ml of deionized water was added to a solution of 7.57 g of $KMnO_4$ (0.045 mol) in 38 ml of deionized water and 4 ml of concentrated HNO_3. The mixed solution was refluxed at 100 °C for 24 h, and the product was filtered, washed, and dried at 120 °C. The dried sample was calcined at 400 °C for 4 h and denoted as OMS-2 in the text. Cu/OMS-2 catalysts with different loadings of CuO were prepared by an incipient wetness method. The support was immerged with a proper amount of $Cu(NO_3)_2$ solution. The slurry was heated at 80 °C under stirring for 15 min to remove the water, followed by a calcination at 400 °C for 4 h in air. The resulting catalysts were denoted as CuO2.5/OMS-2, CuO5/OMS-2, CuO10/OMS-2, CuO15/OMS-2, and CuO20/OMS-2, with the num-

* Corresponding author. Tel.: +86 579 82283910; fax: +86 579 82282595.
E-mail address: mengfeiluo@zjnu.cn (M.-F. Luo).

1385-8947/$ – see front matter © 2010 Elsevier B.V. All rights reserved.
doi:10.1016/j.cej.2010.05.015

ber referring to the mass percentage of CuO in the catalyst (CuO + OMS-2).

For comparison, MnO_x support was prepared by a deposition method. A detailed process is as follows: an aqueous solution of KOH (2 M) was added to an aqueous solution of $MnSO_4$ under stirring until a precipitate was obtained. The resulting precipitate was aged at 50 °C for 1 h, and then separated from the mother liquid by centrifugation. The solid was washed with deionized water and dried at 120 °C overnight. Finally, it was calcined at 400 °C for 4 h. CuO15/MnO_x catalyst was prepared by an impregnation method with the same procedure as the CuO/OMS-2, followed by a calcination at 400 °C for 4 h in air. The CuO loading in this catalyst was 15 wt%.

2.2. Characterization

The specific surface areas (S_{BET}) of the catalysts were measured from a multipoint Braunauer–Emmett–Teller (BET) analysis of the nitrogen adsorption isotherms at 77 K recorded on an Quantachrome Autosorb-1 apparatus.

The scanning electron microscopy (SEM) images were taken on a Hitachi S-4800 scanning electron microscope (SEM) operated at 1 kV. The samples were dispersed into ethanol with ultrasonic treatment for 5 min, and drops of the suspension were placed on a copper sheet for SEM observations. The transmission electron microscopy (TEM) images of the catalysts were obtained on a JEM2010 microscope operated at 200 kV. The sample was dispersed into ethanol with ultrasonic treatment for 5 min, and drops of the suspension were placed on a copper grid for TEM observations.

The X-ray diffraction (XRD) patterns were collected on a PANalytical X'Pert PRO MPD powder diffractometer using Cu Kα radiation (λ = 0.1542 nm). The working voltage was 40 kV and the current was 40 mA. The intensity data were collected at 25 °C in a 2θ range from 10° to 90°, with a scanning speed of 0.7° s^{-1} and a step of 0.03°. The lattice parameters and crystallite size of the samples were determined by the Rietveld method, using JADE 6.5 software.

The X-ray photoelectron spectroscopy (XPS) measurements were performed on a Kratos AXIS Ultra DLD high performance electron spectrometer using nonmonochromatized Al Kα excitation source ($h\nu$ = 1486.6 eV). Binding energies were calibrated by using the contaminant carbon (C 1s = 284.6 eV).

The elemental compositions of catalysts were determined by X-ray fluorescence (XRF) analysis equipped with ARL ADVANT'X Intelli Power 4200 scanning X-ray fluorescence spectrometer. The results were analyzed using UniQuant non-standard sample quantitative analysis software.

The reducibility of the catalysts was measured by the hydrogen temperature-programmed reduction (H_2-TPR) technique. A 15 mg of the sample was placed in a quartz reactor which was connected to a homemade TPR apparatus and the reactor was heated from 40 °C to 700 °C with a heating rate of 10 °C min^{-1}, in a reducing atmosphere of mixed H_2 (5 vol.%) and N_2 (95 vol.%) with a total flow rate of 30 ml min^{-1}. The amount of H_2 uptake during the reduction was measured by a thermal conductivity detector (TCD), calibrated by using a known amount of pure CuO powder. To determine the oxidation state of Mn in the samples, MnO was assumed to be the final state after the hydrogen reduction at temperature lower than 700 °C.

The CO temperature-programmed desorption (CO-TPD) measurements were carried out in a fixed-bed quartz tubular reactor equipped with a quadrupole mass spectrometer (Omnistar, Balzers). 15 mg of sample was loaded and heated to 400 °C with an Ar flow (30 ml min^{-1}) and kept at this temperature for 30 min. After cooling down to room temperature, CO adsorption was done by passing a 5 vol.% CO in Ar mixture (30 ml min^{-1}) through the sample for 30 min, and the sample was purged with Ar (30 ml min^{-1}) for 1 h. The system was then heated to 400 °C with a ramp of 10 °C min^{-1} in Ar flow (30 ml min^{-1}). The desorbed CO_2 was monitored by the mass spectrometer with a m/e of 44.

Diffuse reflectance infrared Fourier transform (DRIFT) spectra of the samples were recorded using a Nicolet 670 spectrometer equipped with a MCT detector and a DRIFTS cell (Harrick), under reaction conditions with a resolution of 4 cm^{-1}. An accumulation of 32 scans was used for collecting background spectrum and 8 scans for collecting sample spectrum. About 20 mg of the catalyst which was ground in an agate mortar for 5 min was placed in the cell and pretreated at 400 °C for 0.5 h in a flow of He (30 ml min^{-1}) in order to remove water and carbonate in the catalyst. Subsequently, the system was cooled down to 30 °C and the background spectrum was recorded. After the introduction of the gas mixture (1% CO in Ar) for 10 min, the spectra were collected. The catalyst was purged with He for 20 min to remove the physisorbed CO, then the spectra were collected at 30 °C.

2.3. Catalytic activity measurement

The CO oxidation was performed in a quartz tubular (i.d. = 6 mm) fixed-bed reactor under atmospheric pressure. A 200 mg of the catalyst was loaded in the reactor. The reaction temperature was monitored by a thermocouple placed in the middle of the catalyst bed. A mixture of 1 vol.% CO and 1 vol.% O_2 balanced by N_2 was introduced as the reactants. The total flow rate was 40 ml min^{-1}, corresponding to a space velocity of 12,000 ml g^{-1} h^{-1}. The CO and CO_2 were analyzed by an on-line GC (Shimadzu GC2014) equipped with a FID detector and two columns (carbon molecular sieves and TDX-502). The gaseous products passed through a methanization converter filled with Raney-Ni catalyst and all the carbon-containing products were converted to methane before they went to the FID detector to ensure a high intensity of signal.

Conversion of CO was calculated as follows:

$$\text{CO conversion}\,(\%) = \frac{[\text{CO}]_{\text{in}}\ \text{vol.\%} - [\text{CO}]_{\text{out}}\ \text{vol.\%}}{[\text{CO}]_{\text{in}}\ \text{vol.\%}} \times 100$$

where $[CO]_{out}$ and $[CO]_{in}$ are the CO concentrations in the products (vol.%) and feed gas (vol.%), respectively. Carbon balance is near 100%.

3. Results

3.1. Structural characterization

The BET surface areas of catalysts are summarized in Table 1. It can be seen that the surface areas of the OMS-2 is 93 m^2 g^{-1}. The surface areas of the supported CuO catalysts are slightly lower than those of the support. The BET surface area of MnO_x is 29 m^2 g^{-1}, which is much lower than that of the OMS-2.

The actual content of CuO in the catalysts is listed in Table 1. It shows that the actual CuO content in the catalyst is very close to the nominal value since the catalyst was prepared using an impregnation method.

Fig. 1 shows the SEM and TEM images of the catalysts. The OMS-2 exhibits nanorod-shaped morphologies, with diameters of about 13 nm and lengths of 400–500 nm. In contrast, the MnO_x exhibits spherical particles with a diameter of about 150 nm. The HRTEM image of OMS-2 (Fig. 1c) indicates that the distance between the lattice fringes is 0.692 nm, which corresponds to the d-spacing of the (1 1 0) plane of MnO_2.

Fig. 2a shows the XRD patterns of the CuO/OMS-2 and OMS-2 catalysts. The diffraction peaks at 2θ of 12.6°, 17.9°, 28.7°, 37.5°, 41.9°, 49.9°, and 60.1° are attributed to the crystalline phase of cryptomelane (KMn_8O_{16}), indicating that the nanorod OMS-2 material

Table 1
BET surface area, CuO content, phase compositions and crystallite sizes of catalysts with different CuO loadings.

Catalyst	BET surface area ($m^2\ g^{-1}$)	CuO content [a] (wt%)	Phase composition	Crystallite size (nm)
OMS-2	93	–	MnO_2	11.1
CuO2.5/OMS-2	91	2.53	MnO_2	10.6
CuO5/OMS-2	92	4.91	MnO_2	10.8
CuO10/OMS-2	88	9.87	MnO_2 + CuO	10.2 (MnO_2)
CuO15/OMS-2	74	14.76	MnO_2 + CuO	9.7 (MnO_2) + 16 (CuO)
CuO20/OMS-2	70	19.92	MnO_2 + CuO	10 (MnO_2) + 19 (CuO)
CuO15/MnO_x	23	14.72	Mn_3O_4 + Mn_5O_8 + CuO	2.8 (Mn_3O_4) + 11.5 (Mn_5O_8) + 11 (CuO)
MnO_x	29	–	Mn_3O_4 + Mn_5O_8	45.6 (Mn_3O_4) + 25.5 (Mn_5O_8)

[a] Determined by XRF.

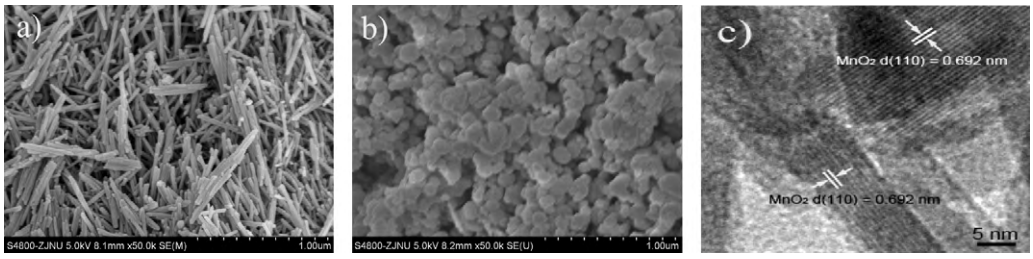

Fig. 1. SEM images of (a) OMS-2, (b) MnO_x, and HRTEM images of (c) OMS-2.

has a cryptomelane-type structure [18]. However, XRD peaks due to CuO are not detected in the samples with CuO loading lower than 10%, indicating that CuO species may be highly dispersed in these samples or the crystallite size of the CuO is below threshold detection limit of the XRD apparatus. For CuO10/OM-2 catalyst, weak diffraction peaks of CuO are observed, and the intensities of these peaks increase with increasing CuO loading from 10 to 20%, which indicates the growth of CuO crystallites. Fig. 2b shows the XRD patterns of the CuO15/MnO_x and MnO_x catalysts. It can be seen that the characteristic peaks of Mn_3O_4 and Mn_5O_8 are observed in these catalysts, and characteristic peaks for CuO are observed in the CuO15/MnO_x.

The results of crystallite size and phase compositions determined by he Rietveld method using JADE 6.5 software are also summarized in Table 1. The results show that the crystallite size of CuO increases with increasing CuO loading, while that of MnO_2 is still about 10 nm in OMS-2.

3.2. Surface and redox properties of the catalysts

In order to investigate the surface properties of these catalysts, XPS measurements were performed. Fig. 3a shows the XPS spectra of Mn 2p in the catalysts. The detailed peak fitting results are listed in Table 3. It is found that these samples contain both Mn^{3+} and Mn^{4+} species [19,20]. For the CuO15/MnO_x catalyst, it is found that the binding energies of Mn $2p_{3/2}$ and Mn $2p_{1/2}$ are essentially identical to those of MnO_x support. However, compared to those of the support OMS-2, the binding energies of the Mn 2p of the CuO15/OMS-2 catalyst are 0.4 eV higher, indicating an interaction between CuO and OMS-2 support. Quantitative analysis of the sur-

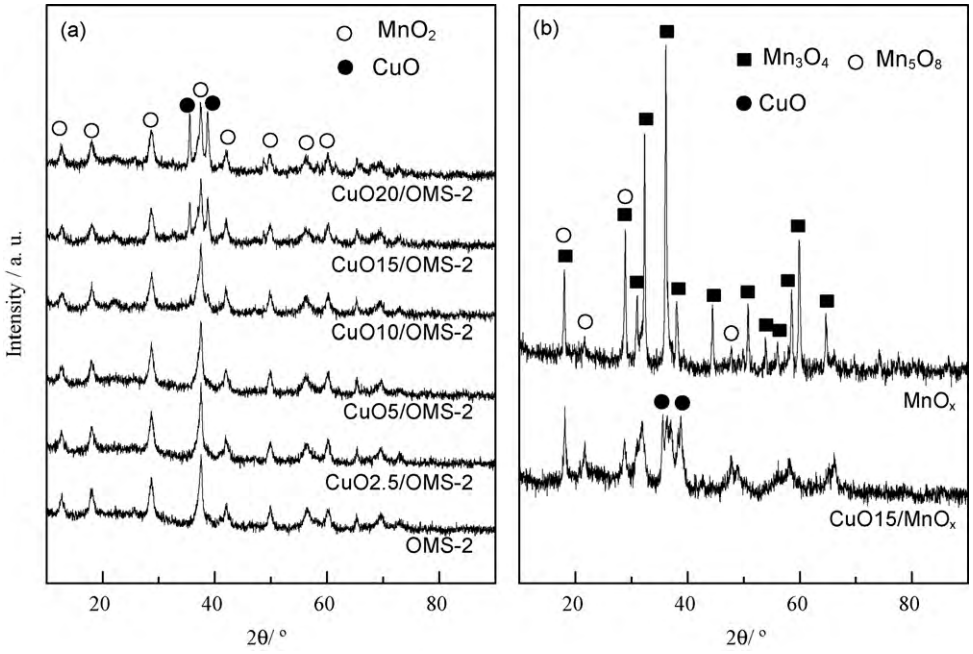

Fig. 2. XRD patterns of (a) catalysts with different CuO loadings and (b) CuO15/MnO_x and MnO_x catalysts.

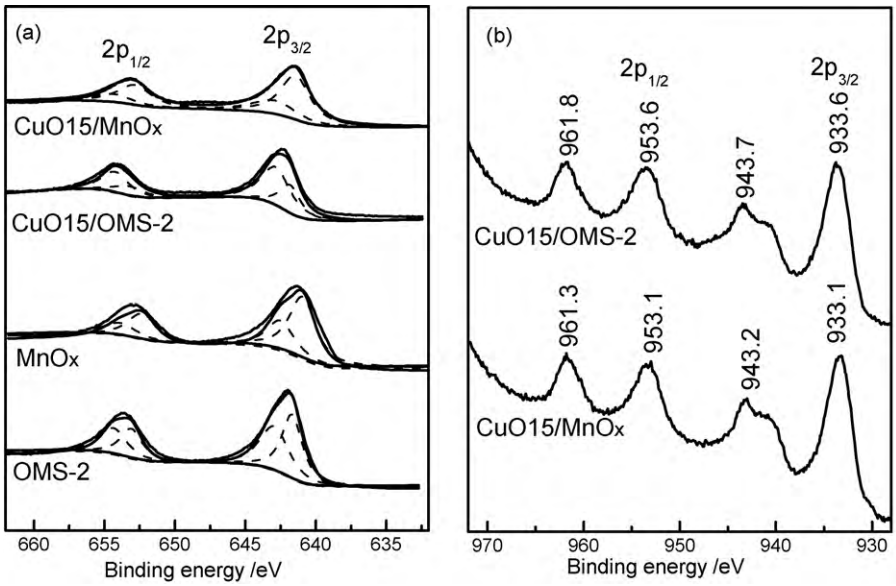

Fig. 3. XPS spectra of (a) Mn 2p in CuO15/OMS-2, CuO15/MnO_x, OMS-2 and MnO_x catalysts and (b) Cu 2p in CuO15/OMS-2 and CuO15/MnO_x catalysts.

face components shows that the OMS-2 and CuO15/OMS-2 samples contain more Mn^{4+} (about 50%) than the MnO_x and CuO15/MnO_x (about 30%), indicating that Mn species in the OMS-2 have higher average oxidation state than the MnO_x. Also, it is found that the surface Cu contents in the CuO containing catalysts (about 40%, atomic ratio) are higher than the nominal contents (about 20%), indicating that the CuO may enrich on the catalyst surface.

Fig. 3b shows the Cu 2p XPS of CuO15/OMS-2 and CuO15/MnO_x catalysts. For the CuO15/MnO_x catalyst, the main peaks are observed at BE ($2p_{1/2}$) = 953.1 eV and BE ($2p_{3/2}$) = 933.1 eV, accompanied by shake-up satellites at BE ($2p_{1/2}$) = 961.3 eV and BE ($2p_{3/2}$) = 943.2 eV, respectively. For the CuO15/OMS-2 catalyst, the main peaks are observed at BE ($2p_{1/2}$) = 953.6 eV and BE ($2p_{3/2}$) = 933.6 eV, accompanied by shake-up satellites at BE ($2p_{1/2}$) = 961.8 eV and BE ($2p_{3/2}$) = 943.7 eV, respectively. These results show that Cu^{2+} species are present on the surface of catalysts [21]. The Cu 2p binding energies for the CuO15/OMS-2 are higher than those for CuO15/MnO_x, which indicates an interaction between CuO and OMS-2.

The redox properties of the catalysts are measured by means of H_2-TPR. Fig. 4a shows the H_2-TPR profiles of the CuO/OMS-2 catalysts. For all catalysts, two reduction peaks (γ_1 and γ_2) at 200–450 °C are observed. These two peaks correspond to the typical two-step reduction process of MnO_2: the first step (peak γ_1) is ascribed to the reduction of MnO_2/Mn_2O_3 to Mn_3O_4, and the second step (peak γ_2) is ascribed to the reduction of Mn_3O_4 to MnO [22,23]. For the CuO/OMS-2 catalysts, the reduction peaks (γ_1 and γ_2) shift to lower temperatures, indicating that the presence of copper promotes the reducibility of manganese oxide through a hydrogen spillover effect [24]. In addition, two new peaks (α, β) appear in the temperature range of 130–300 °C. The α peak centered at 180 °C is usually assigned to the reduction of the finely dispersed CuO parti-

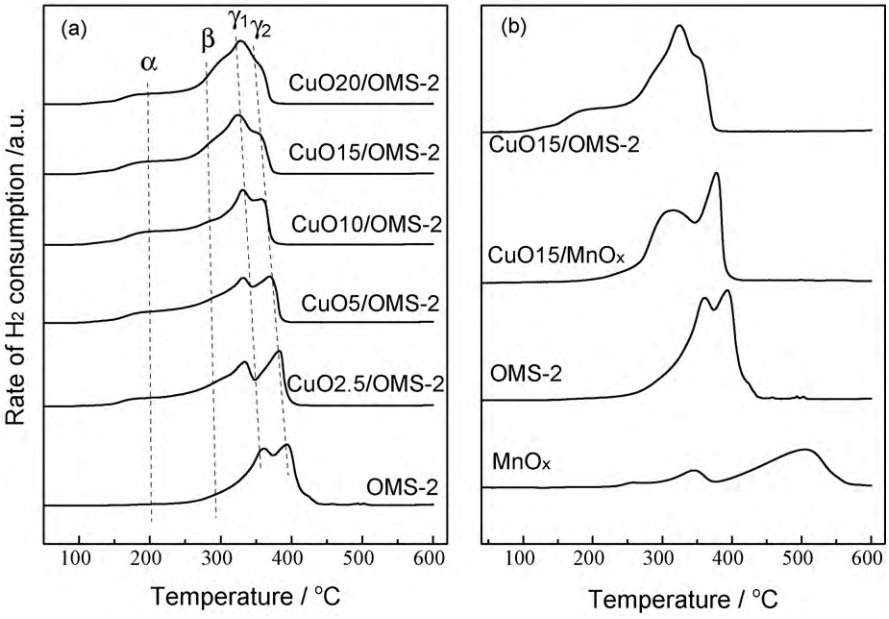

Fig. 4. H_2-TPR profiles of (a) CuO/OMS-2 and OMS-2 and (b) CuO15/OMS-2, CuO15/MnO_x, OMS-2 and MnO_x.

Table 2
Comparison of nominal H_2 consumption and peak α.

Catalyst	H_2 consumption ($\times 10^{-3}$ mmol g cat^{-1})	
	Nominal[a]	α peak[b]
CuO2.5/OMS-2	6	25
CuO5/OMS-2	12	48
CuO10/OMS-2	24	50
CuO15/OMS-2	48	55
CuO20/OMS-2	96	46

[a] Based on the CuO content in the catalyst.
[b] Based on the calibrated H_2 consumption of CuO powder.

cles, while the β peak centered at 275 °C is assigned to the reduction of large CuO particles [6,7,10]. The amount of H_2 consumption of peak α calculated from the TPR profile is listed in Table 2. It can be seen that the H_2 consumption for the α peak of the CuO/OMS-2 catalyst is much larger than the corresponding nominal H_2 consumption of the CuO in the catalyst (except for the CuO20/OMS-2), indicating that the α peak includes not only the reduction of finely dispersed CuO particles but also partial reduction of MnO_2 species. The enhanced reduction of MnO_2 is due to the spillover of hydrogen from Cu atoms to manganese oxides. Furthermore, the reduction peak α suggests an interaction between the finely dispersed CuO particles and MnO_2, which greatly enhances the mobility of oxygen. Actually, similar phenomenon has been found in an Ag-OMS-2 system. Chen et al. assigned the reduction peak of Ag-OMS-2 catalysts at low temperature (109 °C) to the combined reduction of Ag^+ to Ag and MnO_2 to Mn_3O_4 [16]. With respect to the high temperature reduction peak (peak β), it is probably due to a combined reduction of large CuO particles and MnO_2 to Mn_3O_4 [16].

Fig. 4b shows the H_2-TPR profiles for the MnO_x, OMS-2 and supported CuO catalysts. The MnO_x support shows one reduction peak centered at 340 °C and one weak reduction peak at 505 °C. The former is due to the reduction of Mn_5O_8 to Mn_3O_4, while the latter is due to the reduction of Mn_3O_4 to MnO [25]. For the supported CuO15/MnO_x catalyst, the reduction peaks shift to the lower temperatures at 310 and 380 °C. The first reduction peak is related to a combined reduction of large CuO particles to Cu and Mn_5O_8 to Mn_3O_4, and the second reduction peak is related to Mn_3O_4 to MnO [26]. Compared to the CuO15/OMS-2 catalyst, the low-temperature reduction peak α is absent in the CuO15/MnO_x catalyst, indicating that the CuO15/MnO_x catalyst barely contains finely dispersed CuO particles.

3.3. Catalytic activity for CO oxidation

Fig. 5 shows the catalytic activities of the catalysts for CO oxidation. The reactivity of the OMS-2 or MnO_x support is quite low, and the OMS-2 shows slightly higher activity than the MnO_x. With the addition of CuO, the activities of the supported catalysts are remarkably enhanced. For the CuO/OMS-2 catalysts, the catalytic activity increases with increasing CuO loading from 2.5 to 5 wt%. However, with further increasing CuO loading (from 5 to 15 wt%), the catalytic activity hardly changes, when CuO loading increases

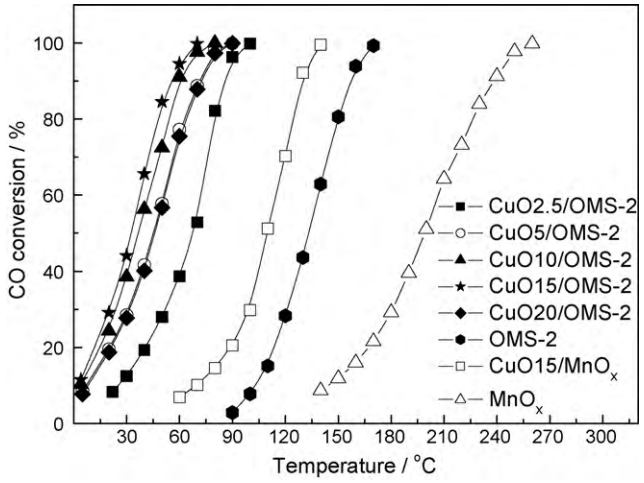

Fig. 5. CO oxidation over CuO/OMS-2 and CuO/MnO_x catalysts.

to 20 wt%, the activity slightly declines. Among the catalysts, the highest reactivity is obtained on the CuO15/OMS-2 catalyst, with a T_{90} (the lowest temperature for 90% conversion of CO) of 55 °C. And 45% conversion of CO is obtained even at 30 °C. Moreover, it is found that the CuO15/OMS-2 is also much more active than the CuO15/MnO_x. The CuO/OMS-2 catalysts in the current work show slightly higher catalytic activities than other Cu-based mixed oxides reported elsewhere for the oxidation of CO to CO_2 at low temperatures [27,28]. The activity of CuO15/OMS-2 is also higher than that of CuO–CeO_2 catalysts reported in our previous work [10]. Also, CO oxidation under high O_2 concentration (20% in air) was carried out on the CuO15/OMS-2 catalyst. It was found that the reactivity of the catalyst was almost unchanged, implying that the catalyst may be applicable to the realistic reaction condition.

4. Discussion

4.1. Roles of Cu^{2+}–O–Mn^{4+} entities in the CO oxidation

The introduction of CuO in both OMS-2 and MnO_x supports greatly improves the activities of catalysts. For the CuO/OMS-2 catalysts, the promoting effect of CuO is even more pronounced, and the introduction of CuO makes the T_{90} decreases by 103 °C (from 158 °C to 55 °C). It is interesting that the CuO15/OMS-2 catalyst has much higher activity than the CuO15/MnO_x, which implies that the differences in the structural and chemical properties of these two supports greatly affect the catalytic behavior. The porous structure of the OMS-2 material may facilitate the diffusion of the reactants. In other hand, the average oxidation state of Mn species in the OMS-2 material is relatively higher than that in the MnO_x (Table 3), which may cause discrepancies in the catalytic behavior as many literatures pointed out that Mn species with high oxidation state are beneficial to the oxidation reaction [29]. More importantly, the differences in the structural and chemical properties of these two

Table 3
Surface analysis of catalysts by XPS measurements.

Catalyst	BE (eV)				$Mn^{4+}/(Mn^{4+}+Mn^{3+})$ (atomic %)	Cu/Mn atomic ratio
	Mn^{3+}		Mn^{4+}			
	$2p_{3/2}$	$2p_{1/2}$	$2p_{3/2}$	$2p_{1/2}$		
CuO15/OMS-2	641.8	653.2	643.1	654.4	51	0.41
CuO15/MnO_x	641.5	652.9	643.2	654.6	31	0.43
OMS-2	641.8	653.2	643.1	654.4	50	–
MnO_x	641.1	652.5	642.8	654.2	32	–

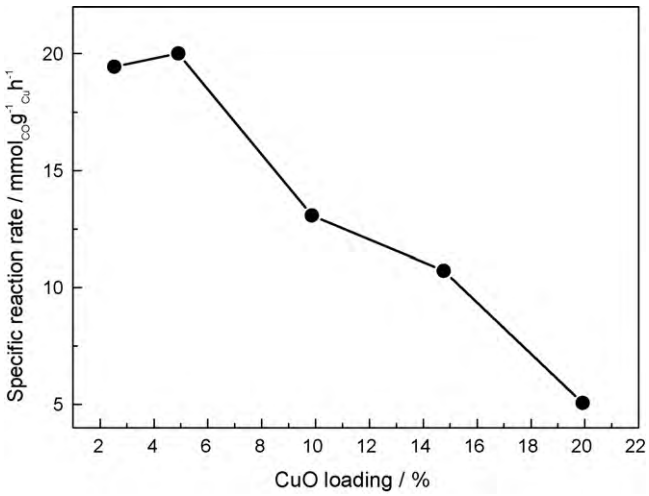

Fig. 6. Specific reaction rate based on Cu loading in CuO/OMS-2 catalysts at reaction temperature of 20 °C.

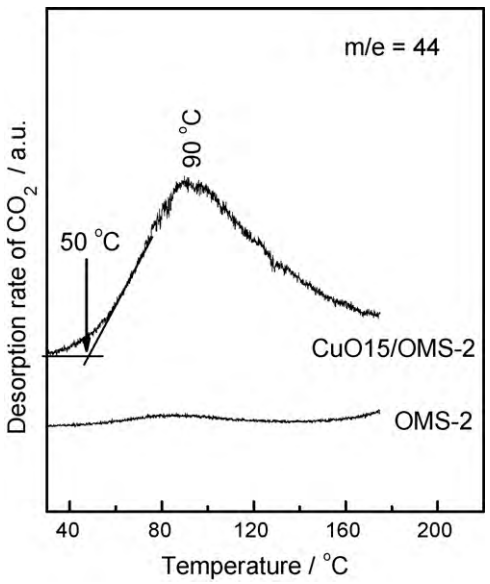

Fig. 7. CO-TPD profiles of CuO15/OMS-2 and OMS-2 catalysts.

supports would affect the interaction between the CuO and the Mn species. Note that the TPR profiles of the CuO/OMS-2 contain a low-temperature reduction peak (α) starting from 130 °C, representing a combined reduction of finely dispersed CuO particles and MnO_2. The presence of this low-temperature reduction peak implies an interaction between the finely dispersed CuO particles and the OMS-2 support, probably due to a Cu^{2+}–O–Mn^{4+} entity [30]. But no reduction peak at the temperature region of 130–200 °C was observed for the CuO15/MnO_x catalyst. Moreover, the XPS results show that the binding energies of the Mn 2p of the CuO15/OMS-2 catalyst are 0.4 eV higher than that of OMS-2. This suggests an interaction between the CuO and OMS-2, which most probably occurs at the CuO-OMS-2 interface. Ramstad and Mikkelsen [31] proposed that the presence of octahedral Mn^{4+} and Cu^{2+} ions were supposed to interact with lattice oxygen. The interaction of the Mn–O and Cu–O bond makes the oxygen species more negative, which is favorable for easy activation of oxygen species.

In order to compare the intrinsic reaction activities of these catalysts, reaction rates of the CuO/OMS-2 catalysts based on the weight of Cu in the catalyst ($mmol_{CO}\ g_{Cu}^{-1}\ h^{-1}$) for CO oxidation at 20 °C were calculated and the results are shown in Fig. 6. And it is found that the reaction rates are close for the low CuO loading catalysts (CuO2.5/OMS-2 and CuO5/OMS-2), but higher CuO loading in the catalyst results in a decline of reaction rates. The calculated specific rates based on CuO loading in the catalyst reflect the contribution of the finely dispersed CuO particles to the reaction. As the XRD results clearly show that the catalysts with low CuO loading contain finely dispersed CuO particles; while those with high CuO loadings have large CuO particles, leading to a lower fraction of finely dispersed CuO particles in these catalysts, thus the reaction rate is suppressed. Interestingly, it is found that the catalysts with similar reduction peak areas (peak α in Table 2) have very close reactivities (Fig. 5). This finding suggests that the Cu^{2+}–O–Mn^{4+} entities possesses an easily reducible bridge oxygen that generates from an interaction of the finely dispersed CuO particles and the MnO_2 support, which are responsible for the reactivity, particularly in the low-temperature region. The reducible bridge oxygen was also found in Ag-OMS-2 systems [32,33]. Meanwhile, the absence of the low-temperature reduction peak in the CuO15/MnO_x catalyst implies the lack of the interacted Cu^{2+}–O–Mn^{4+} entities, which can interpret the low activity of the CuO15/MnO_x in the low-temperature region.

Fig. 7 shows the CO-TPD profile of the CuO15/OMS-2 and OMS-2 catalysts. For the CuO15/OMS-2, a low-temperature desorption peak started at 50 °C appears. For the OMS-2, a very weak desorption peak is observed at the temperature range of 60–100 °C. This indicates that the CO adsorbed on the surface of CuO/OMS-2 is very easy to react with the active lattice oxygen species to form CO_2 [26], while that adsorbed on the OMS-2 support reacts with the active lattice oxygen species at higher temperature.

4.2. Possible reaction mechanism for CO oxidation

For the CO oxidation on transition metal oxides such as MnO_x, Co_3O_4 and Fe_2O_3, a Mars-van-Krevelen mechanism is proposed [34]. The reaction pathway involves the incorporation of the lattice oxygen in the support oxide with CO and the reduced oxide on the surface could be re-oxidized by free oxygen in the feed gas. Therefore, the mobility/reducibility of the active lattice oxygen is of crucial importance for the reaction. Pu et al. [35] proposed that the oxygen vacancies provide activation centers for O_2 and the Cu species provide chemisorption sites for CO oxidation.

By combining the reducible lattice oxygen in the Cu^{2+}–O–Mn^{4+} entities and the activities of CuO/OMS-2 catalysts for CO oxidation at low temperatures, a reaction pathway of CO oxidation on CuO/OMS-2 could be proposed as follows:

$$2Cu^{2+}\text{–}O^{2-}\text{–}Mn^{4+} + 2CO \rightarrow 2Cu^{+}\text{–}\square\text{–}Mn^{3+} + 2CO_2$$

$$2Cu^{+}\text{–}\square\text{–}Mn^{3+} + O_2 \rightarrow 2Cu^{2+}\text{–}O^{2-}\text{–}Mn^{4+}$$

$$2CO + O_2 \rightarrow 2CO_2$$

where □ represents an oxygen vacancy.

The very reducible bridge oxygen in the Cu^{2+}–O^{2-}–Mn^{4+} entity could react with CO to produce CO_2 and a partially reduced Cu^{+}–□–Mn^{3+} couple; then the Cu^{+}–□–Mn^{3+} entities could be re-oxidized rapidly by O_2 in the feed gas. This reaction pathway is similar to that reported on the Cu–Ce–O catalyst for CO oxidation. For example, Marbán and Fuertes [36] proposed a Cu^{2+}–O^{2-}–$Ce^{4+} \leftrightarrow Cu^{+}$–□–$Ce^{3+} + (1/2)O_2$ redox couple to explain the reaction mechanism.

In addition, to prove the process of Cu^{+}–□–Mn^{3+} entities can be re-oxidized rapidly, the CuO15/OMS-2 catalyst was reduced from 40 °C to 200 °C (1st TPR), and the catalyst was re-oxidized at 50 °C in the feed O_2 gas for 1 h, then was reduced from 40 °C to 200 °C again (2nd TPR). The H_2-TPR profiles (Fig. 8a) show about 50% of the CuO15/OMS-2 catalyst is re-oxidized to Cu^{2+}–O^{2-}–Mn^{4+}. Therefore, the Cu^{+}–□–Mn^{3+} entities could be re-oxidized rapidly at 50 °C, which confirms the process of

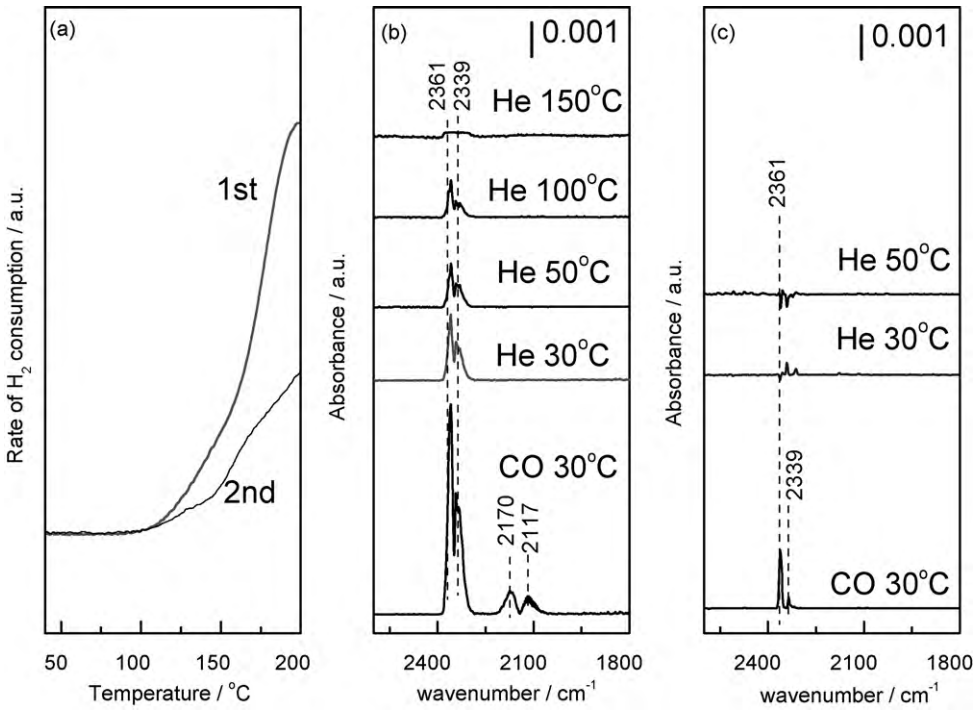

Fig. 8. (a) H_2-TPR profiles of CuO15/OMS-2 the 1st time and the 2nd time; (b) in situ DRIFT spectra for CO chemisorption over CuO15/OMS-2; (c) in situ DRIFT spectra for CO chemisorption over OMS-2 support.

Cu^{2+}–O^{2-}–Mn^{4+} ↔ Cu^{+}–□–Mn^{3+} + O_2 could cycle easily. Moreover, Fig. 8b shows the in situ DRIFT spectra of CO absorption over the catalyst of CuO15/OMS-2. It can be seen there are two peaks at 2117 and 2170 cm^{-1}, however, when the catalyst is purged with He, the two peaks disappear. Therefore, these two peaks are attributed to gaseous CO [37]. The peaks at 2300 to 2400 cm^{-1}, assigned to the adsorbed CO_2 and the gaseous CO_2 [37], are observed for the CuO15/OMS-2 catalyst even at 30 °C. The results of the in situ DRIFT indicate that CO could react easily on the surface of catalysts to produce CO_2 even at 30 °C, and the CO_2 adsorbed on the catalysts' surface. With increasing temperature, CO_2 desorbes from the catalysts' surface. When the temperature increases to 150 °C, the peak disappears. Fig. 8c shows the in situ DRIFT spectra of CO absorption over the OMS-2 support. Compared to the CuO15/OMS-2 catalyst, the intensity of the formed gaseous CO_2 is much weaker on the support. This phenomenon is in good accordance with the CO-TPD results (Fig. 7). It can be concluded that adsorbed CO could react easily with active oxygen species on surface, and Cu^{+}–□–Mn^{3+} entities could be re-oxidized rapidly to complete the redox cycle.

5. Conclusions

Cu/OMS-2 catalysts exhibit high CO oxidation activities, and the lowest temperature for 90% conversion of CO is 55 °C. The interaction between the highly dispersed CuO and OMS-2 support generates active sites for CO oxidation. CO oxidation may follow the Mars-van-Krevelen mechanism with Cu^{2+}–O^{2-}–Mn^{4+} ↔ Cu^{+}–□–Mn^{3+} + O_2 redox couple.

References

[1] H.Q. Zhu, Z.F. Qin, W.J. Shan, W.J. Shen, J.G. Wang, J. Catal. 225 (2004) 267–277.
[2] X.C. Zheng, X.L. Zhang, Z.Y. Fang, X.Y. Wang, S.R. Wang, S.H. Wu, Catal. Commun. 7 (2006) 701–704.
[3] M.A. Bollinger, M.A. Vannice, Appl. Catal. B 8 (1996) 417–443.
[4] A. Wolf, F. Schüth, Appl. Catal. A 226 (2002) 1–13.
[5] D.R. Schryer, B.T. Upchurch, B.D. Sidney, K.G. Brown, G.B. Hoflund, R.K. Herz, J. Catal. 130 (1991) 314–317.
[6] M.F. Luo, Y.J. Zhong, X.X. Yuan, X.M. Zheng, Appl. Catal. A 162 (1997) 121–131.
[7] M.F. Luo, Y.P. Song, J.Q. Lu, X.Y. Wang, Z.Y. Pu, J. Phys. Chem. C 111 (2007) 12686–12692.
[8] C.S. Chen, J.H. You, J.H. Lin, Y.Y. Chen, Catal. Commun. 9 (2008) 2381–2385.
[9] W. Liu, M. Flytzani-Stephanopoulos, J. Catal. 153 (1995) 304–316.
[10] M.F. Luo, J.M. Ma, J.Q. Lu, Y.P. Song, Y.J. Wang, J. Catal. 246 (2007) 52–59.
[11] Y.F. Shen, R.P. Zerger, R.N. Deguzman, S.L. Suib, L. McCurdy, D.I. Potter, C.L. O'Young, Science 260 (1993) 511–515.
[12] A. Dyer, M. Pillinger, J. Newton, R. Harjula, T. Möller, S. Amin, Chem. Mater. 12 (2000) 3798–3804.
[13] M. Abecassis-Wolfovich, R. Jothiramalingam, M.V. Landau, M. Herskowitz, B. Viswanathan, T.K. Varadarajan, Appl. Catal. B 59 (2005) 91–98.
[14] A.R. Gandhe, J.S. Rebello, J.L. Figueiredo, J.B. Fernandes, Appl. Catal. B 72 (2007) 129–135.
[15] F. Schurz, J.M. Bauchert, T. Merker, T. Schleid, H. Hasse, R. Gläser, Appl. Catal. A 355 (2009) 42–49.
[16] J.L. Chen, J. Li, H.J. Li, X.M. Huang, W.J. Shen, Microporous Mesoporous Mater. 116 (2008) 586–592.
[17] R.N. DeGuzman, Y.F. Shen, E.J. Neth, S.L. Suib, C.L. O'Young, S. Levine, J.M. Newsam, Chem. Mater. 6 (1994) 815–821.
[18] S. Sithambaram, E.K. Nyutu, S.L. Suib, Appl. Catal. A 348 (2008) 214–220.
[19] M. Oku, K. Hirokawa, S. Ikeda, J. Electron Spectros. Relat. Phenomena 7 (1975) 465–473.
[20] J.H. Ge, L.H. Zhuo, F. Yang, B. Tang, L.Z. Wu, C.H. Tung, J. Phys. Chem. B 110 (2006) 17854–17859.
[21] D.V. Cesar, C.A. Peréz, M. Schmal, V.M.M. Salim, Appl. Surf. Sci. 157 (2000) 159–166.
[22] H. Trevino, G.D. Lei, W.M.H. Sachtler, J. Catal. 154 (1995) 245–252.
[23] R. Xu, X. Wang, D.S. Wang, K.B. Zhou, Y.D. Li, J. Catal. 237 (2006) 426–430.
[24] M.R. Morales, B.P. Barbero, L.E. Cadús, Fuel 87 (2008) 1177–1186.
[25] J. Papavasiliou, G. Avgouropoulos, T. Ioannides, J. Catal. 251 (2007) 7–20.
[26] C.S. Chen, W.H. Cheng, S.S. Lin, Appl. Catal. A 238 (2003) 55–67.
[27] J.B. Wang, D.H. Tsai, T.J. Huang, J. Catal. 208 (2002) 370–380.
[28] A. Martínez-Arias, A.B. Hungría, M. Fernández-García, J.C. Conesa, G. Munuera, J. Phys. Chem. B 108 (2004) 17983–17991.
[29] S. Imamura, M. Shono, N. Okamoto, A. Hamada, S. Ishida, Appl. Catal. A 142 (1996) 279–288.
[30] Z.Q. Zou, M. Meng, L.H. Guo, Y.Q. Zha, J. Hazard. Mater. 163 (2009) 835–842.
[31] A.L. Ramstad, Ø. Mikkelsen, J. Mol. Struct. 697 (2004) 109–117.
[32] W. Gac, Appl. Catal. B 75 (2007) 107–117.
[33] G.G. Xia, Y.G. Yin, W.S. Willis, J.Y. Wang, S.L. Suib, J. Catal. 185 (1999) 91–105.
[34] J. Jansson, J. Catal. 194 (2000) 55–60.
[35] Z.Y. Pu, X.S. Liu, A.P. Jia, Y.L. Xie, J.Q. Lu, M.F. Luo, J. Phys. Chem. C 112 (2008) 15045–15051.
[36] G. Marbán, A.B. Fuertes, Appl. Catal. B 57 (2005) 43–53.
[37] A. Martínez-Arias, M. Fernańdez-García, O. Gálvez, J.M. Coronado, J.A. Anderson, J.C. Conesa, J. Soria, G. Munuera, J. Catal. 195 (2000) 207–216.